44. Y. Shigetani *et al.*, *Science* **296**, 1316 (2002).
45. S.-H. Lee, K. K. Fu, J. N. Hui, J. M. Richman, *Nature* **414**, 909 (2001).
46. C. B. Kimmel, C. T. Miller, R. J. Keynes, *J. Anat.* **199**, 105 (2001).
47. M. Cohn, *Nature* **416**, 386 (2002).
48. This work was supported by research grants to J. R. from Nina Ireland, the March of Dimes, and National Institute of Mental Health (K02MH01046-01), and to M. D. from ARCS (Achievement Rewards for College Scientists) Foundation and National Institute of Dental Research (T32DE07204). Ours thanks to J. Brunet, J. Drouin, G. Karsenty, K. Mahon, A. McMahon, F. Meijlink, T. Nakamura, E. Olson, and P. Sharpe for probes, and the Rubenstein lab, E. Depew, and J. Depew for commentary.

Supporting Online Material
www.sciencemag.org/cgi/content/full/1075703/DC1
Figs. S1 to S3

2 July 2002; accepted 14 August 2002
Published online 22 August 2002;
10.1126/science.1075703
Include this information when citing this paper.

Nanometer Resolution and Coherent Optical Dipole Coupling of Two Individual Molecules

C. Hettich,[1] C. Schmitt,[1] J. Zitzmann,[2] S. Kühn,[2] I. Gerhardt,[2] V. Sandoghdar[2]*

By performing cryogenic laser spectroscopy under a scanning probe electrode that induces a local electric field, we have resolved two individual fluorescent molecules separated by 12 nanometers in an organic crystal. The two molecules undergo a strong coherent dipole-dipole coupling that produces entangled sub- and superradiant states. Under intense laser illumination, both molecules are excited via a two-photon transition, and the fluorescence from this doubly excited system displays photon bunching. Our experimental scheme can be used to optically resolve molecules at the nanometer scale and to manipulate the degree of entanglement among them.

Optical studies with nanometer spatial resolution have been plagued by the diffraction limit in microscopy. However, recently it has been noted that so long as two point-like emitters are not fully identical, they can be distinguished in the optical detection process regardless of their separation (*1*). A few experiments have explored this by taking advantage of different emission or absorption wavelengths of the neighboring emitters (*2*, *3*). By analyzing the intensity distribution of the image spots, one can locate the center of each emitter with a great lateral accuracy limited by the available signal-to-noise ratio. We have achieved nanometer three-dimensional sensitivity by replacing such intensity images with the Stark-shift maps that are obtained if a sample containing molecules with narrow zero-phonon lines (*4*) is scanned in an inhomogeneous electric field. After identifying two closely spaced molecules, we performed quantum optical measurements to investigate the coherent interaction between the dipole moments associated with their optical transitions. Furthermore, we demonstrate the feasibility of on-command modification of the degree of entanglement between these two molecules and discuss possibilities for the manipulation of larger ensembles.

Identification of two individual molecules. Fluorescence excitation spectroscopy (*5*) was performed at temperature $T \simeq 1.4$ K to detect single terrylene molecules embedded in a para-terphenyl crystal with a thickness of about 250 nm (*6*). At this temperature, the linewidth of the zero-phonon transition connecting the singlet ground and excited states becomes lifetime-limited, so that at low doping concentrations the spectra of different molecules in a small excitation volume no longer overlap. Therefore, as the frequency of a dye laser [wavelength $(\lambda) \simeq 578$ nm, linewidth $(\Delta\nu) \simeq 1$ MHz] is scanned through the inhomogeneous absorption band of terrylene, single molecules are excited one after another. An excited molecule then decays at the rate γ^{00} by the zero-phonon line and at the rate γ^{St} by the Stokes-shifted transitions to the vibrational states of the electronic ground state. This fluorescence was collected by a high-numerical-aperture objective (NA = 0.8) and was passed through a filter that blocks the emission on the zero-phonon line as well as the scattered light from the excitation laser. By scanning the laser frequency and recording the number of Stokes-shifted photons at the detector, we obtained narrow lifetime-limited spectral lines associated with single molecules.

In our cryostat, we used the stage of a scanning near-field microscope to position a local probe in the immediate vicinity of a sample (*7*). The probe consisted of a polymer microsphere (diameter of 3 μm) that was attached to the end of a sharp fiber tip and then coated with silver to serve as an electrode (Fig. 1A). The backside of the substrate containing the sample was coated with a few nanometers of gold and served as a grounded counterelectrode, so that the application of a voltage to the tip created a strongly inhomogeneous electric field in the crystal. Once a molecular resonance was identified in the fluorescence excitation spectra, the crystal was raster-scanned and the position-dependent Stark shift of the resonance was recorded. By analyzing the spatiospectral map that was obtained, we located the corresponding molecule with an accuracy on the order of 1 nm (*8*).

We then searched for molecules that were spaced by much less than one wavelength and found two resonances, *I* and *J* (Fig. 1B), that displayed nearly identical Stark maps, indicating two such molecules. We set the distance between the probe's extremity and the crystal's upper surface to about 370 nm, scanned the sample in *x* and *y* directions, and recorded the Stark shift of both resonances *I* and *J* simultaneously at each pixel. Figure 1C represents the Stark shift of resonance *I*, and the symbols in Fig. 1D display all of its cross sections along the *x* axis at different *y* values. In order to determine the lateral separation between the centers of the Stark maps for the two resonances, we first performed a linear interpolation of the data for the shift of resonance *J* and then fit the resulting surface function to the data of resonance *I* by displacing it. The cross sections of this function are shown by the blue curves in Fig. 1D. The remaining residues of less than a molecular linewidth are displayed by the black curves and not only confirmed the robustness of this fit but also allowed us to determine that the lateral distance between the dipole moments associated with the two resonances is $\sqrt{(x_I - x_J)^2 + (y_I - y_J)^2} \simeq 5 \pm 2$ nm. We then positioned the microsphere at the center of the map in Fig. 1C and recorded more Stark spectra for both resonances while varying the sphere-sample distance *z*. The red squares in Fig. 1E show the shift of resonance *I*, and the curve in Fig. 1F displays the difference between the frequency shifts of resonances *I* and *J* as a function of *z*. We again deduced the displacement $(z_I - z_J)$ by

---

[1] Department of Physics, University of Konstanz, 78457 Konstanz, Germany. [2] Physical Chemistry Laboratory, Swiss Federal Institute of Technology (ETH), CH-8093 Zurich, Switzerland.

*To whom correspondence should be addressed. E-mail: vahid.sandoghdar@ethz.ch

11 October 2002

Science

Vol. 298 No. 5592
Pages 311–482 $10

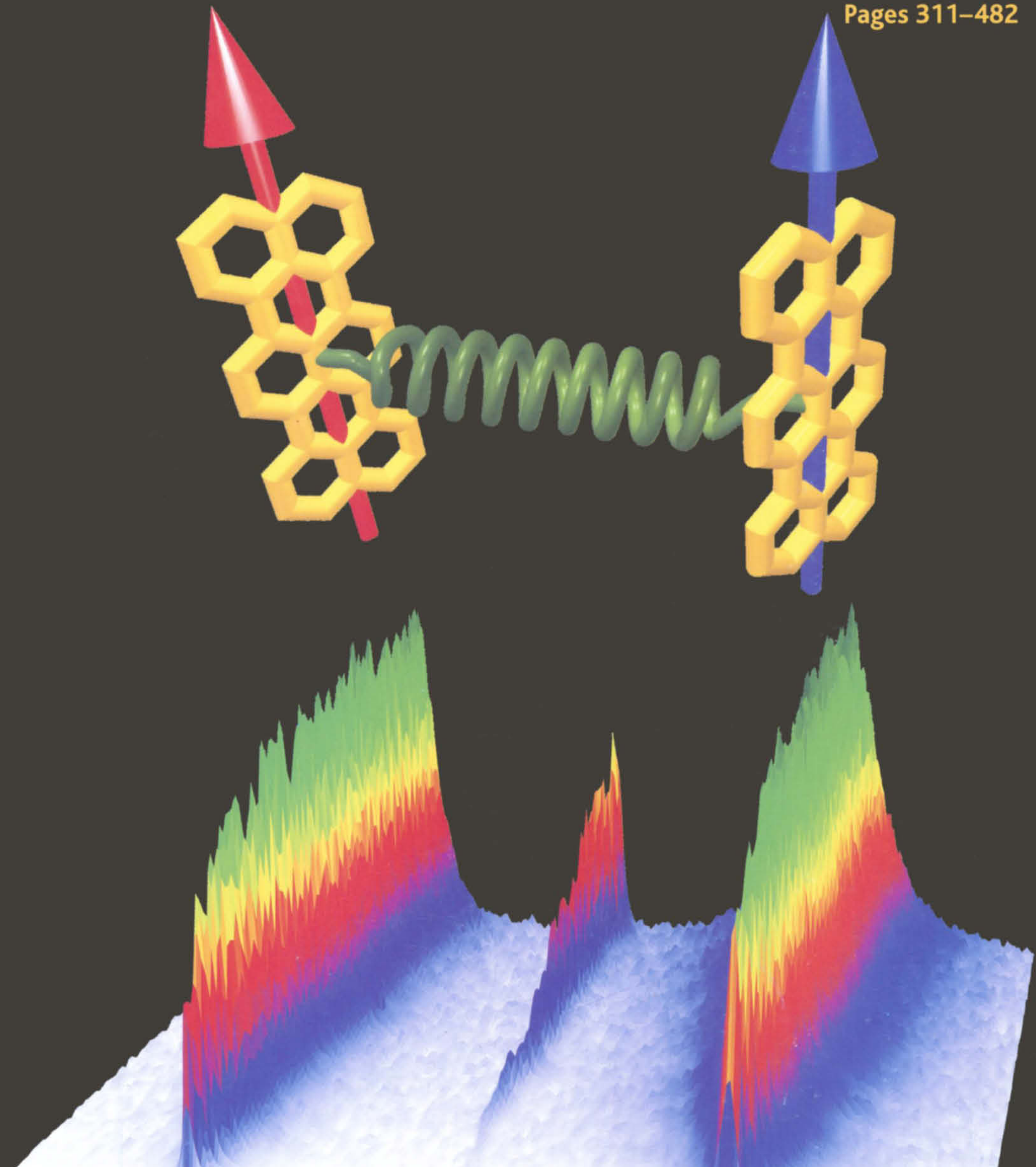

American Association for the Advancement of Science

fitting the linear interpolation of the data for resonance *J* (see the solid blue curve in Fig. 1E) to those of resonance *I*. As depicted in Fig. 1G, the tight tolerance in this fit leaves a very small residue, yielding $(z_I - z_J) \simeq 7.5 \pm 1$ nm. Therefore, we deduce the separation of the dipole moments associated with the two resonances to be $r_{IJ} \simeq 9 \pm 2$ nm.

The dipole-dipole interaction between the molecules. Having established the very small separation of the two dipole moments, we searched for evidence of the dipole-dipole coupling in the spectral properties of the system when the local probe was retracted. As has been known in magnetic resonance spectroscopy (*9*) and optical ensemble experiments (*10*), cooperative effects induced by the dipole coupling among particles can lead to multiphoton processes. We increased the excitation laser intensity by two orders of magnitude and observed the evolution of the spectrum displayed in Fig. 1B (Fig. 2). The appearance of a new peak at high intensities midway between the two original resonances is evidence for dipole-dipole coupling and arises through the two-photon excitation of both molecules (*11*, *12*).

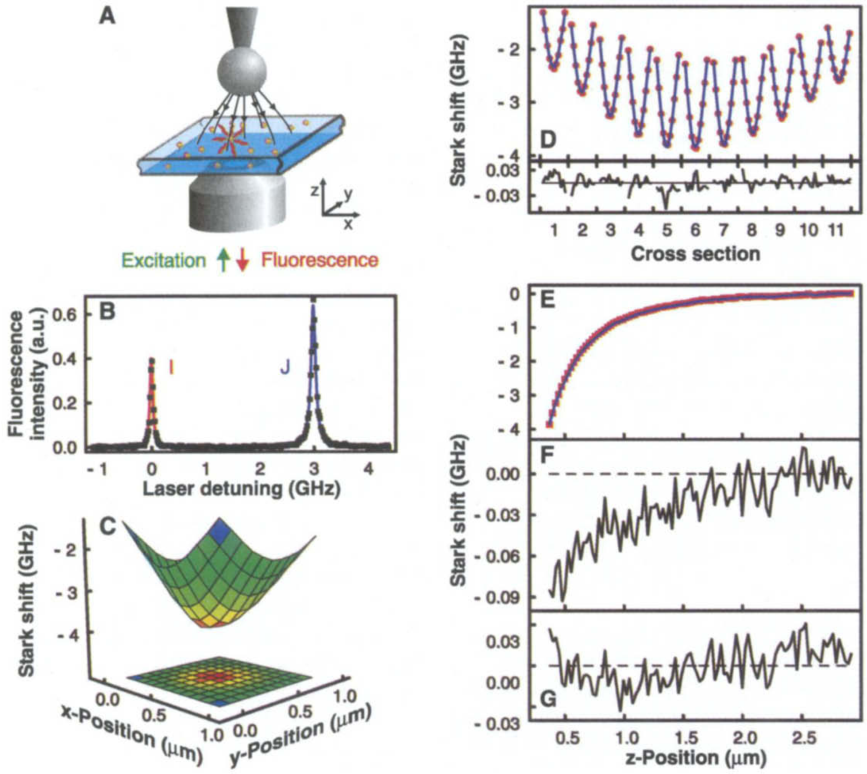

Fig. 1. (**A**) A diagram of the experimental arrangement at $T \simeq 1.4$ K. By using a scanning electrode containing a sphere with a diameter of 3 µm, we apply a local inhomogeneous electric field on a thin crystal. A microscope objective is used to illuminate the molecules and collect their fluorescence. As the crystal is raster-scanned, the guest molecules inside experience position-dependent Stark shifts. (**B**) The fluorescence signal as a function of the excitation laser frequency is plotted, showing the two resonances *I* and *J* that are studied in this work. a.u., arbitrary units. (**C**) A two-dimensional map of the Stark shift of resonance *I* as a function of *x* and *y*. The projection of this surface function is also shown. (**D**) Here the 11 cross sections along the *x* axis are plotted one after the other. The symbols represent the experimental data, and the solid curves through them show the fit described in the text. The black curves in the lower section display the remaining residue between the symbols and the fit. (**E**) The red symbols show the *z* dependence of the Stark shift for resonance *I* when the microsphere was laterally centered on the molecules. The blue curve is the linear interpolation of the Stark shift for resonance *J* after being fitted to the values of *I*. (**F**) The difference in raw frequency shifts of resonances *I* and *J* at each *z*. (**G**) The small residue that remains after fitting the symbols by the blue solid line in (E).

Fig. 2. Excitation spectra for a wide range of laser intensities. A linear offset has been subtracted in order to eliminate the contribution of the background fluorescence at high excitation intensities.

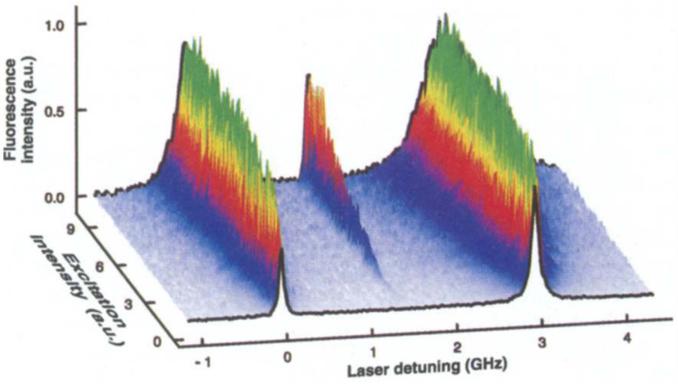

Before we present the quantitative discussion of the spectra in Fig. 2, it is appropriate to set some theoretical grounds. Consider two two-level molecules that are separated by the vector $\vec{\mathbf{r}}_{12}$ and possess transition dipole moments $\vec{\mathbf{d}}_i \equiv \langle g_i|\vec{\mathbf{D}}_i|e_i\rangle$, dipole operators $\vec{\mathbf{D}}_i$, transition frequencies ν_i, and spontaneous emission rates γ_i with $i = 1,2$. In the near field, the dipole-dipole interaction energy $h\delta_{12}$ of the system (where h is Planck's constant) is given by (*13*)

$$h\delta_{12} = \frac{3h\sqrt{\gamma_1\gamma_2}}{8\pi(k_0 n r_{12})^3} \cdot [(\hat{\mathbf{d}}_1 \cdot \hat{\mathbf{d}}_2) - 3(\hat{\mathbf{d}}_1 \cdot \hat{\mathbf{r}}_{12})(\hat{\mathbf{d}}_2 \cdot \hat{\mathbf{r}}_{12})] \qquad (1)$$

where $k_0 c = 2\pi\nu_0 \equiv 2\pi(\nu_1 + \nu_2)/2$ and n denotes the index of refraction of the medium. As sketched in Fig. 3A, two molecules coupled in this manner can be considered as a four-level system with the ground state $|G\rangle = |g_1 g_2\rangle$, the upper state $|U\rangle = |e_1 e_2\rangle$, and the intermediate superposition states $|I\rangle = b|e_1 g_2\rangle - a|g_1 e_2\rangle$ and $|J\rangle = a|e_1 g_2\rangle + b|g_1 e_2\rangle$, where the coefficients a and b are determined by diagonalizing the new full Hamiltonian (*12*). The frequencies of the coupled system then read $\nu_G = 0$ and

$$\nu_{I,J} = \nu_0 \mp \sqrt{\left(\frac{\nu_2 - \nu_1}{2}\right)^2 + \delta_{12}^2}$$

$$\nu_U = \nu_1 + \nu_2 \qquad (2)$$

As pointed out by Dicke (*14*), the interaction between the two molecules is also expected to modify their spontaneous emission rates, because the existence of one dipole in the near field of the other opens an additional decay channel. For very small separations, the single-photon emission rates of the new excited states can be readily obtained by calculating the Einstein A coefficient (*15*) $\gamma = 2\omega^3|\vec{\mathbf{d}}|^2/(3\varepsilon_0 hc^3)$ (where ε_0 is the vacuum permittivity) in conjunction with the matrix elements of the total dipole operator $\vec{\mathbf{D}}_s = \vec{\mathbf{D}}_1 + \vec{\mathbf{D}}_2$ for the system. The outcome of this simple calculation is in excellent agreement with the rigorous solutions of a master equation

(16) and is given by

$$\gamma_I = b^2\gamma_1 + a^2\gamma_2 - 2ab\gamma_{12},$$
$$\gamma_J = a^2\gamma_1 + b^2\gamma_2 + 2ab\gamma_{12},$$
$$\gamma_U = \gamma_1 + \gamma_2. \qquad (3)$$

Here γ_{12} denotes the incoherent cross-damping rate (13), which for $k_0 r_{12} \ll 1$ takes the form $\gamma_{12} = \sqrt{\gamma_1\gamma_2}\,(\hat{\mathbf{d}}_1 \cdot \hat{\mathbf{d}}_2)$. The positive and negative contributions of $2ab\gamma_{12}$ in Eq. 3 stem from the constructive and destructive interference of the decay channels of the two molecules, portraying the essence of Dicke's superradiance and subradiance.

To examine our data more quantitatively, we calculated the steady-state density matrix ρ from the full master equation (16), treating two nonidentical two-level molecules that undergo dipole-dipole coupling and interact with a laser field (12, 13). In our calculations, we take $\gamma_1 = \gamma_2$ (17), but we let $\nu_1 < \nu_2$ because of the inhomogeneous distribution of transition frequencies in the crystal. Furthermore, the strong phonon coupling of the excited vibrational states destroys the coherence of the dipole moments associated with γ^{St}, so that the corresponding dipoles in the two molecules do not undergo an efficient coherent coupling with each other. Therefore, we have only considered the coupling of the dipole moments connected with γ^{00} and have replaced γ_1 and γ_2 by γ^{00} in the definitions of δ_{12} and γ_{12} and by $\gamma^{\mathrm{tot}} = \gamma^{00} + \gamma^{\mathrm{St}}$ in cases where the total emission rate is asked for in the master equation. Finally, we have allowed the upper state $|U\rangle$ to be shifted by $\Delta\nu_U$, in addition to the consequences of the dipole-dipole interaction.

The experimental spectra can be simulated by summing over the products of the new excited state populations with their respective decay rates, yielding the number of emitted photons at each excitation frequency. However, we present the results in the uncoupled basis $\{|g_1g_2\rangle, |e_1g_2\rangle, |g_1e_2\rangle, |e_1e_2\rangle\}$ because it provides insight into the nontrivial distribution of populations between the two molecules. The populations $\rho_{eg,eg} = \langle e_1g_2|\rho|e_1g_2\rangle$, $\rho_{ge,ge} = \langle g_1e_2|\rho|g_1e_2\rangle$, and $\rho_{ee,ee} = \langle e_1e_2|\rho|e_1e_2\rangle$ are plotted (Fig. 3B) for the parameters of the spectrum displayed in full in Fig. 3C, corresponding to the highest excitation intensity of Fig. 2. The pink curve in Fig. 3C shows that we can reproduce and fit the experimental data by plotting the quantity $(\rho_{eg,eg} + \rho_{ge,ge} + 2\rho_{ee,ee})$, which is proportional to the probability of emitting a Stokes-shifted photon. The excitation of a single molecule is now no longer confined to a particular frequency. Instead, we see how the various curves in Fig. 3B add to produce well-defined resonances at eigenfrequencies ν_I and ν_J. Of particular interest is the green curve, which confirms that both molecules can be excited simultaneously via a two-photon process at the central resonance frequency (see also Fig. 3A).

The symbols and the solid curves in Fig. 4 summarize all of the experimental and theoretical values for the peak intensities (Fig. 4A), linewidths (Fig. 4B), and center frequencies (Fig. 4C) of the spectra (18) in Fig. 2. The very good agreement between theory and experiment allows us to determine the fit parameters to be $\delta_{12} \simeq +0.95$ GHz, $(\nu_2 - \nu_1)/2 \simeq 1.16$ GHz, $\gamma^{\mathrm{tot}}/2\pi \simeq 50$ MHz, and $\gamma_{12}/2\pi \simeq 9$ MHz, corresponding to coefficients $a = 0.34$ and $b = 0.94$ in the composition of $|I\rangle$ and $|J\rangle$. The early saturation of the two resonances at ν_I and ν_J in Fig. 4A suggests a measure for the high excitation intensities needed for the appearance of the central peak that then grows in a nonlinear fashion. As indicated in Fig. 4B, the linewidth of resonance J is always greater than that of I. Indeed, a close scrutiny of the resonances recorded at a very low excitation intensity reveals a linewidth of 44 (± 4) MHz for I and 57 (± 4) MHz for J. Considering Eq. 3 and that $\gamma^{\mathrm{tot}}_{1,2}/2\pi \simeq 50$ MHz, these values are in very good agreement with our analysis that $2ab(\gamma_{12}/2\pi) = 6$ MHz and provide clear spectral evidence of subradiance and superradiance. Furthermore, the initial linewidth of the central resonance equals 50 (± 1) MHz, which also agrees well with the prediction $\gamma_U = \gamma_1 + \gamma_2$ of Eq. 3 if we note that in a two-photon process, the apparent linewidth in an excitation frequency scan is always half the transition linewidth.

As shown in Fig. 4C, the resonance frequencies do not depend on the laser power.

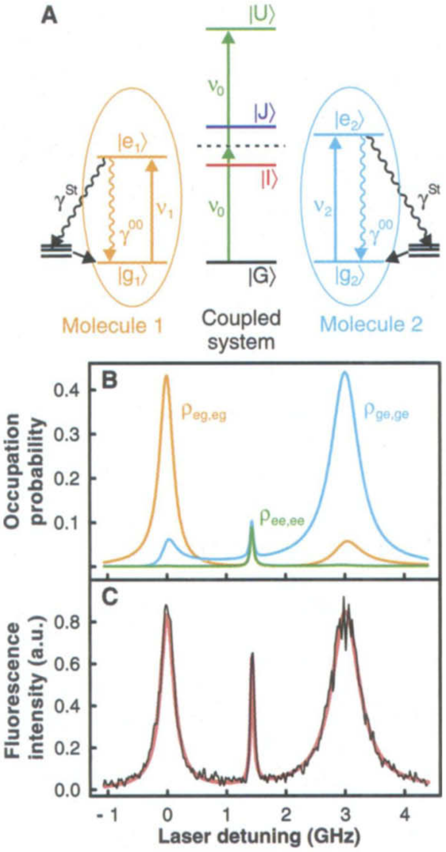

Fig. 3. (**A**) Two two-level molecules with ground states $|g_1\rangle$, $|g_2\rangle$ and excited states $|e_1\rangle$, $|e_2\rangle$ are represented by the encircled systems. The coupled system of the two molecules can be treated as a new four-level system, with the ground state $|G\rangle$, intermediate states $|I\rangle$ and $|J\rangle$, and the upper state $|U\rangle$. In the case of terrylene, the excited state can decay at the rate γ^{00} via the zero-phonon channel or at the rate γ^{St} via the Stokes-shifted transitions to the vibrational levels of the ground state. Because these transitions are followed by very fast decay to the ground state, they do not contribute to the coherent coupling between the molecules. (**B**) The red, blue, and green curves display an example of the distribution of populations $\rho_{eg,eg}$, $\rho_{ge,ge}$, and $\rho_{ee,ee}$ among the ground and excited states of the two molecules for different laser frequencies. (**C**) The black curve shows an experimental spectrum, whereas the pink curve is obtained when $(\rho_{eg,eg} + \rho_{ge,ge} + 2\rho_{ee,ee})$ is calculated and plotted using the optimal fit parameters. The left and the right peaks mark the eigenfrequencies of the entangled states $|I\rangle$ and $|J\rangle$.

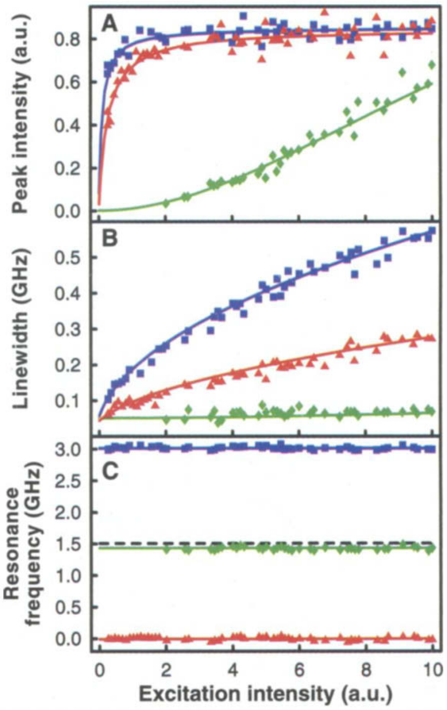

Fig. 4. (**A**) Peak intensities, (**B**) linewidths, and (**C**) center frequencies of the three resonances in Fig. 2 are displayed over about two orders of magnitude of variation in excitation intensity. The triangles and squares show the experimental data for the resonances at ν_I and ν_J, respectively, and the diamonds represent the central resonance. The solid curves plot the corresponding quantities extracted from the theoretical fit to the data. The dashed line in (C) marks the algebraic average of ν_I and ν_J and emphasizes the small deviation of the data from this value due to the matrix-assisted shift of $\Delta\nu_U \simeq -160$ MHz in the doubly excited state $|U\rangle$.

However, there is a clear deviation $\Delta\nu_U$ of the central frequency from ν_0, represented by the dashed line where the two-photon excitation should take place, according to a theory based on the dipole-dipole interaction; thus, we have allowed for this offset in the theory in a phenomenological manner. Having verified that this shift appears in all of the measurements of the two molecules and having checked all of potential sources of systematic effects in the experiment as well as data analysis, we believe that this shift belongs to the class of excitation-induced frequency shifts (*19*, *20*). As discussed by Brown and Orrit (*20*), a possible mechanism at work is that excitation of one molecule slightly changes the size of its electronic clouds, exerting a local pressure on a nearby molecule and therefore shifting its energy levels. If both molecules are excited, each induces a shift $\Delta\nu_U/2$ on the other, and as a result the upper state is detuned by an amount $\Delta\nu_U$. The fits to our experimental data arrive at $\Delta\nu_U \simeq -160$ MHz, which is in good agreement with the estimates of Brown and Orrit.

Photon statistics of the coupled molecules. Further evidence for dipole-dipole coupling was provided by the measurement of time-resolved photon statistics of the fluorescence emitted from the coupled system (*21*, *22*). For this measurement, we split the fluorescence light onto two avalanche photodiodes and obtain the autocorrelation function

$$g^{(2)}(\tau) = \frac{\langle I(t)I(t+\tau)\rangle}{\langle I(t)\rangle^2} = \frac{\langle I(t+\tau\,|\,t)\rangle}{\langle I(t)\rangle} \quad (4)$$

by plotting the histogram of the consecutive counts on the two detectors at time intervals τ. Here the brackets denote averaging over time t, and $I(t + \tau | t)$ stands for the signal intensity at time $t + \tau$ if a photon has been detected at t. To facilitate integration over longer times, we scanned the laser frequency in a small region around the value of interest. As is the case for a single emitter (*23*), we observe photon antibunching when we illuminate the system at ν_I where only one photon can be absorbed (Fig. 5A). However, the excitation of the central resonance leads to a photon-bunching phenomenon (Fig. 5B), which fully supports the interpretation that the dipole-dipole coupling allows for the simultaneous excitation of both molecules followed by the emission of two photons at very short time intervals. This is in contrast to the photon-antibunched fluorescence that would be emitted from two uncoupled molecules (*23*). In order to compare our results with the predictions of the theory, we derived $g^{(2)}(\tau)$ by considering the time evolution of the density matrix after having been reset because of the emission of the first photon (*24*). In these calculations, we have taken into account the experimentally measured value of the background fluorescence, which becomes important at very high excitation intensities, and we have summed over contributions for different excitation frequencies to model laser frequency scanning. The solid curve in Fig. 5B shows that the result coincides very well with the experimental curve without any fit parameters.

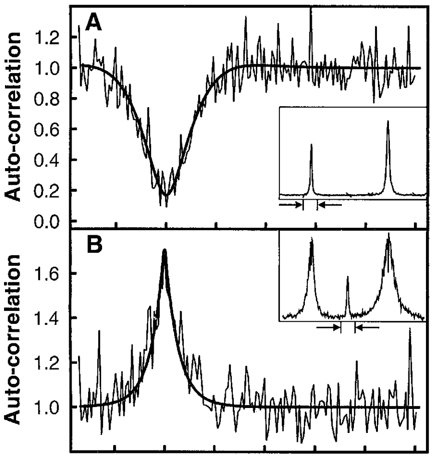

Fig. 5. The autocorrelation function $g^{(2)}(\tau)$ is plotted. Antibunching is obtained when the laser is scanned about the lower resonance (**A**), whereas bunching is obtained by scanning about the central peak (**B**). In each case, the spectra corresponding to the system under study and the frequency region contributing to the data are shown in the inset. The smooth curves display the calculated $g^{(2)}(\tau)$ without any fit parameters.

Nanometer resolution of molecules and manipulation of the degree of entanglement between them. Let us now return to the issue of spatial coordinates of the two molecules. Earlier we showed that the spacing between the dipole moments associated with resonances I and J is 9 nm. Having analyzed the dipole-dipole interaction between the molecules, we note that the mixing of their internal states renders them indistinguishable in frequency space, and therefore the Stark maps of I and J could not yield the positions of the individual molecules directly. To this end, the assessment of their coordinates on the basis of intensity images (*3*) would also introduce systematic errors if the effect of the coupling were neglected. However, having deduced the coupling strength δ_{12} from our spectral data, we can use Eq. 2 to solve for the frequency shifts of individual molecules at any given scan pixel and construct new Stark maps, revealing $\sqrt{(x_1-x_2)^2+(y_1-y_2)^2} \simeq 7 \pm 2$ nm, $(z_1 - z_2) \simeq 10 \pm 1$ nm, and therefore $r_{12} \simeq 12 \pm 2$ nm for the centers of the two molecules. We emphasize that these results do not conflict with the traditional diffraction limit in optical microscopy because we can extract the coupling details of the molecules from spectral studies.

We now consider the possibility of manipulating the degree of entanglement between the molecules through an external influence. One alternative is to apply a differential Stark shift via an inhomogeneous electric field, therefore modifying the frequency detuning $(\nu_J - \nu_I)$ between the entangled states. In fact in our current experiment, this detuning has reached about 90 MHz because of the field gradient in the z direction (Fig. 1F). We also observe similar detunings because of the field gradients in the x and y directions as the sample is scanned laterally. The use of sharper probes and greater electric field gradients could achieve a substantial modification of the energy levels and therefore could control the degree of entanglement between the molecules. Another possibility for manipulating the coupled system of two molecules is to directly tune their dipole-dipole interaction energy by changing their separation $\vec{r}_{12}$ in a scanning probe arrangement where one molecule is placed at the end of a tip and another molecule on a substrate (*7*). Furthermore, by using self-organized systems (*25*, *26*) as templates, one could design arrays of molecules with lattice constants on the order of 10 nm and use our experimental scheme to address the individual units and to control their optical interactions. Aside from an important step toward quantum state engineering (*27*), these experiments would also provide information on existing natural systems, such as light-harvesting complexes, in which excitonic interactions play a central role (*28*).

References and Notes

1. E. Betzig, *Opt. Lett.* **20**, 237 (1995).
2. T. D. Lacoste *et al.*, *Proc. Natl. Acad. Sci. U.S.A.* **97**, 9461 (2000).
3. A. M. van Oijen, J. Köhler, J. Schmidt, M. Müller, G. J. Brakenhoff, *J. Opt. Soc. Am. A* **16**, 909 (1999).
4. W. E. Moerner, M. Orrit, *Science* **283**, 1670 (1999).
5. M. Orrit, J. Bernard, *Phys. Rev. Lett.* **65**, 2716 (1990).
6. V. Sandoghdar *et al.*, *Single Molec.* **2**, 277 (2001).
7. J. Michaelis, C. Hettich, J. Mlynek, V. Sandoghdar, *Nature* **405**, 325 (2000).
8. J. Zitzmann, C. Hettich, I. Gerhardt, V. Sandoghdar, in preparation.
9. R. R. Ernst, G. Bodenhausen, A. Wokaun, *Principles of Nuclear Magnetic Resonance in One and Two Dimensions* (Oxford Univ. Press, Oxford, 1987).
10. F. Varsanyi, G. H. Dieke, *Phys. Rev. Lett.* **7**, 442 (1961).
11. J. R. R. Leite, C. B. de Araujo, *Chem. Phys. Lett.* **73**, 71 (1980).
12. G. V. Varada, G. S. Agarwal, *Phys. Rev. A* **45**, 6721 (1992).
13. U. Akram, Z. Ficek, S. Swain, *Phys. Rev. A* **62**, 13413 (2000).
14. R. H. Dicke, *Phys. Rev.* **93**, 99 (1954).
15. R. Loudon, *The Quantum Theory of Light* (Oxford Univ. Press, Oxford, 1983).
16. G. S. Agarwal, *Springer Tracts in Modern Physics*, G. Höhler, Ed. (Springer-Verlag, New York, 1974), vol. 70, pp. 1–129.
17. S. Kummer, T. Basché, C. Bräuchle, *Chem. Phys. Lett.* **229**, 309 (1994).
18. In the range of the excitation intensities used in the experiment, the resonances in each spectrum show an excellent agreement with a Lorentzian lineshape. Our estimates of the peak intensities, linewidths, and the line frequencies were extracted from Lorentzian fits to the experimental and calculated data.

19. S. B. Altner, M. Mitsunaga, G. Zumofen, U. P. Wild, *Phys. Rev. Lett.* **76**, 1747 (1996).
20. R. Brown, M. Orrit, in *Single Molecule Optical Detection, Imaging and Spectroscopy* (VCH, Weinheim, Germany, 1997), pp. 109–142.
21. T. Richter, *Opt. Acta* **29**, 265 (1982).
22. A. Beige, G. C. Hegerfeldt, *Phys. Rev. A* **58**, 4133 (1998).
23. T. Basché, W. E. Moerner, M. Orrit, H. Talon, *Phys. Rev. Lett.* **69**, 1516 (1992).
24. In our experiment, the detection of a photon is accompanied by populating the molecular ground state via fast decay of vibrational levels. As a result, all of the information about the phase of the system is lost, and we can assume that after the first photon has been detected, the only nonzero elements of the density matrix are the populations $\rho_{eg,eg}$, $\rho_{ge,ge}$, and $\rho_{gg,gg}$.
25. G. Whitesides, B. Grzybowski, *Science* **295**, 2418 (2002).
26. M. E. Davis, *Nature* **417**, 813 (2002).
27. S. Lloyd, *Science* **261**, 1569 (1993).
28. X. Hu, K. Schulten, *Phys. Today* **50**, 28 (1997).

29. We thank C. Henkel and G. Zumofen for fruitful discussions and J. Mlynek for continuous support. We are also grateful to M. Orrit for bringing our attention to the discussion on excitation-induced frequency shifts. The experimental part of this project was performed before we moved from the University of Konstanz, and we thank the Deutsche Forschungsgemeinschaft (SFB 513) as well as the European Union (grant S4P) for financial support.

1 July 2002; accepted 26 August 2002

Published online 5 September 2002;

10.1126/science.1075606
Include this information when citing this paper.

REPORTS

High Abrasion Resistance with Sparse Mineralization: Copper Biomineral in Worm Jaws

Helga C. Lichtenegger,[1]* Thomas Schöberl,[2] Michael H. Bartl,[1] Herbert Waite,[3]* Galen D. Stucky[1]*

Biominerals are widely exploited to harden or stiffen tissues in living organisms, with calcium-, silicon-, and iron-based minerals being most common. In notable contrast, the jaws of the marine bloodworm *Glycera dibranchiata* contain the copper-based biomineral atacamite [$Cu_2(OH)_3Cl$]. Polycrystalline fibers are oriented with the outer contour of the jaw. Using nanoindentation, we show that the mineral has a structural role and enhances hardness and stiffness. Despite the low degree of mineralization, bloodworm jaws exhibit an extraordinary resistance to abrasion, significantly exceeding that of vertebrate dentin and approaching that of tooth enamel.

Most living organisms rely on hard tissues for support, protection, nutrition, and defense. Biomineralization is a major strategy for tissue hardening and manifests an astonishing diversity of bioceramic structures with exquisite microarchitectures that have specially adapted physical properties (*1–6*). Although the variety of architectures seems to be almost infinite, Ca-, Si-, and Fe-based minerals are most common (*7*). As a basic principle, the hardness of these is largely governed by the type of mineral (*8*) and the degree of mineralization (*9*, *10*).

In 1980, Gibbs and Bryan (*11*) first reported copper levels up to 13% w/w in the jaws of the marine polychaete worm *Glycera* sp. Although it was initially suspected that these levels reflected heavy metal pollution at the collection site, jaw composition was found to be remarkably consistent and independent of copper concentration in the seawater. Copper was the most abundant inorganic component; protein, however, was the most predominant constituent (measured as percent of dry weight). The authors concluded that the copper might play a role in mechanically hardening the proteinaceous material. However, no attempt to determine the actual hardness was made nor was the form of the copper further explored.

We show that in *Glycera* jaws, a major part of the copper is deposited as a biomineral. We used a combination of techniques, such as position-resolved synchrotron x-ray diffraction, small-angle scattering, electron microscopy, and nanoindentation to identify the mineral, demonstrate its structural function, and probe the mechanical properties of the jaw. We find that, in spite of the low degree of mineralization, *Glycera* jaws show an extraordinary resistance to abrasion.

Figure 1A shows the image of a *Glycera* jaw as viewed by light microscopy. *Glycera* is armed with a set of four such jaws, each of which is about 1.5 mm long and jet black, with a very sharp, mechanically stable tip that is used by the worm to penetrate the integument of its prey (*12*) and inject venom (*13*). Electron microprobe experiments (*14*) on a ground and polished *Glycera* jaw showed high concentrations of copper in the distalmost tip region (Fig. 1). In accordance with findings by Gibbs and Bryan (1980) (*11*), the copper concentration decreased dramatically from the tip to the base. The local copper distribution in an oblique cross section of the tip is depicted in Fig. 1B (the dark hole in the middle is the venom canal, and the white line circumscribes the outline of the sample). Figure 1C shows the local chlorine distribution. The occurrence of chlorine in the sample was highly correlated with elevated local concentrations of copper (additional chlo-

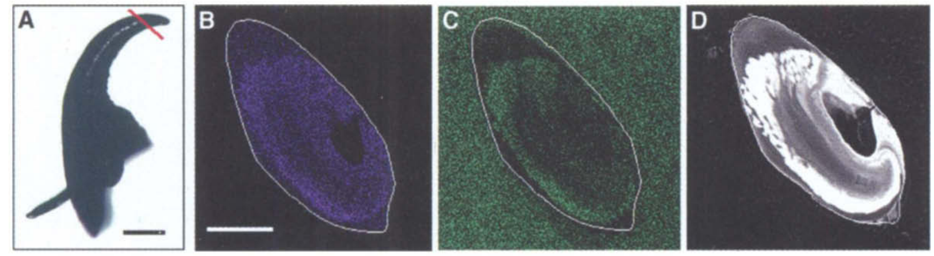

Fig. 1. (**A**) Picture of a *Glycera* jaw under the light microscope. The sharp tip of the jaw is used to penetrate prey integument and inject venom. *Glycera* worms were obtained live from the Marine Biological Laboratory in Woods Hole, Massachusetts, and jaws were dissected from the animal after freezing. The scale bar corresponds to 0.2 mm. The red line denotes the plane of cross section used for element analysis. (**B**) Electron microprobe, copper dot map. The white line denotes the outline of the sample. Scale bar, 50 μm. Regions with higher copper concentration appear bright. The dark region in the middle corresponds to the venom canal. (**C**) Electron microprobe, chlorine dot map. The distribution of chlorine in the sample is highly correlated with the distribution of copper as seen from the copper dot map (additional chlorine around the sample belongs to the epoxy embedding). (**D**) Backscattered electron image. Regions containing high concentrations of elements with larger Z appear bright. The image shows that the inner part of the jaw tip is highly mineralized, in accordance with the element dot map of copper.

---

[1] Department of Chemistry and Biochemistry, University of California, Santa Barbara, CA 93106, USA. [2] Erich Schmid Institute for Materials Science, Austrian Academy of Sciences and University of Leoben, Jahnstrasse 12, A-8700 Leoben, Austria. [3] Department of Molecular, Cellular and Developmental Biology, University of California, Santa Barbara, CA 93106, USA.

*To whom correspondence should be addressed.